Intel Serv Robotics (2015) 8:233–245
DOI 10.1007/s11370-015-0179-9

ORIGINAL RESEARCH PAPER

Design optimization of duct-type AUVs using CFD analysis

Dong-Joon Won[1] · Joonwon Kim[1] · Jinhyun Kim[2]

Received: 25 February 2015 / Accepted: 17 June 2015 / Published online: 10 July 2015

Abstract The purpose of this study was to examine the ideal design for the external and internal shapes of duct-type autonomous underwater vehicles (AUVs) using computational fluid dynamics (CFD). The most important design factors for duct-type AUVs are minimizing the drag force and increasing the thrust because these determine the propulsive efficiency. To improve the propulsive efficiency, the various factors that affect the drag force and thrust of duct-type AUVs were examined. All of the experiments were performed using CFD analysis because physical experiments are inefficient in terms of cost and time. To improve the CFD analysis efficiency, the Taguchi method was used to minimize the number of CFD analyses. Through these processes, design factors that reduce the drag force and increase the thrust according to the external and internal shapes were analyzed. We propose an optimized model that can improve the propulsive efficiency.

Keywords Duct-type autonomous underwater vehicle (AUV) · Computational fluid dynamics (CFD) · Myring equation · Venturi effect

✉ Jinhyun Kim
jinhyun@seoultech.ac.kr

Dong-Joon Won
dongjoonw@postech.ac.kr

Joonwon Kim
joonwon@postech.ac.kr

1 Pohang University of Science and Technology (POSTECH), Pohang, Republic of Korea

2 Seoul National University of Science and Technology (SEOULTECH), Seoul, Republic of Korea

List of symbols

C_D	Drag coefficient
D	Drag force
T	Thrust
u	Inlet flow rate
u_p	Mean flow rate at minimum internal hole diameter of AUV
A_P	Cross-sectional area at minimum internal hole diameter of AUV
A_1	Cross-sectional area at inlet of AUV
A_2	Cross-sectional area at outlet of AUV
V_1	Mean flow rate at inlet of AUV
V_2	Mean flow rate at outlet of AUV
P_1	Mean pressure at inlet of AUV
P_2	Mean pressure at outlet of AUV
P_{ext}	Pressure acting on external shape of AUV
P_{int}	Pressure acting on internal shape of AUV
p	Pressure acting on AUV
a	Length of nose section
b	Length of body section
L	Length of AUV
d	Maximum diameter of hull
θ	Initial angle of tail section
n	Curvature coefficient
ρ	Density of water
ν	Kinematic viscosity coefficient of water
μ	Coefficient of viscosity of water

1 Introduction

Unmanned underwater vehicles (UUVs) are used to perform a variety of tasks, such as the exploration of underwater environments that are difficult for people to reach, maintenance and repair of underwater structures, and explosive mine probing and removal. Their importance continues to grow. UUVs vary in form depending on their purpose and are generally classified depending on whether they have a tether: autonomous underwater vehicles (AUVs) do not have a tether, and remotely operated vehicles (ROVs) do. AUVs are often shaped like torpedoes with a single propeller. They have a streamlined external shape that enables efficient movement and are used to explore a comparatively wide area. However, they have a wide radius of rotation and low capability for postural control; thus, they decline in work efficiency in narrow spaces. In contrast, ROVs have multiple propellers to allow uninhibited control of the hull and an open-frame form for precision-oriented tasks in a local area. However, they move at low speeds and are at a disadvantage with regard to performing tasks in a wide area.

Demand has recently increased for autonomous UUVs that possess both an AUV's high movement efficiency and ROV's low turning radius for use in tasks such as the exploration of complex underwater structures or local regions that are difficult for a person to reach (e.g., inside a nuclear reactor with a high concentration of radioactive wastewater). Research and development is underway to produce underwater robots with a diverse range of forms that meet such demands. The duct-type AUV is an autonomous UUV that can potentially meet the above demands. As shown in Fig. 1, it has a simple structure with a single propeller and offers favorable movement efficiency with a streamlined external shape. Such shapes provide low fluid resistance because most of the fluid flows inside the through-hole; this phenomenon can also improve the propulsive force because the through-hole can be used as a nozzle. Moreover, its short body and small radius of rotation offer favorable work efficiency. Previous work experimentally confirmed that the duct-type AUV has favorable movement efficiency and a small radius of rotation [1], but the shape has not been optimized to enhance the propulsion efficiency. The aim of the present study was to optimize the external and internal shapes of a duct-type AUV using a computational fluid dynamics (CFD) tool.

With recent advances in high-volume, high-performance computational analysis and a variety of optimization design techniques, efforts are continuously being made to optimize the design of different shapes using CFD in terms of time and cost. For example, Kim and Choi [2] optimized the wing-shaped design of a dual-turboprop aircraft with up to 100 seats using the PIAno method, which is a process integration and design optimization tool, for efficient analysis. Through optimization of the aircraft, the directional stability of the tail wing height can be improved, and the wing shape that minimizes the aircraft's drag under cruise conditions with respect to a directionally stable tail wing height can be determined. Kwon et al. [3] optimized the cross-sectional design of a turbine blade to improve the torque and develop a high-efficiency wind power generation system. To optimize the shape, a hybrid genetic algorithm was used to find the most suitable variables for comparison with the initial shape, and the most suitable initial variables were found. For the optimization task, a modified feasible directions algorithm was used. The optimization design process allows a blade to generate a higher torque.

There has been a recent trend toward using CFD for the design of unmanned submersibles beyond these earlier designs [4,5] because underwater experimentation requires a larger-scale circulating water bath and more expensive equipment than experiments performed in air. AUV design has mainly been directed toward enhancing the propulsive efficiency to enable long-term and long-distance operation. Inoue et al. [6] used CFD to enhance the propulsive efficiency of the AUV PICASSO, which was developed at Osaka University. CFD analysis was conducted for six verified models with low drag coefficients at the bow and stern portions. Actual experiments were run and compared to validate the analysis. This resulted in the design of a hull shape with a lower drag coefficient. Jung et al. [7] used CFD to design a

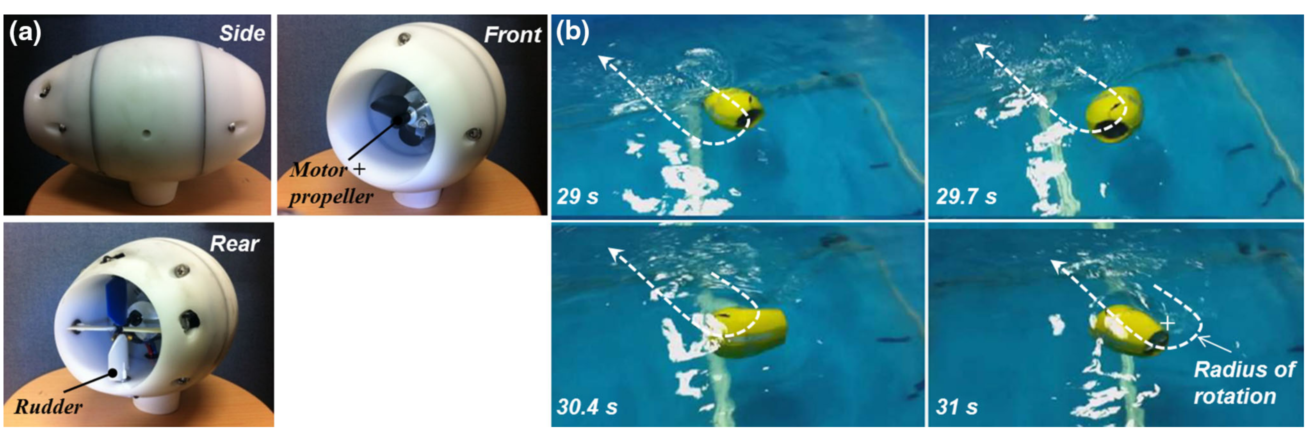

Fig. 1 Duct-type AUV "NEMO" (Navigator & Explorer for Marine Observation) [1]: **a** the motor mounted at the front of the hull generates thrust, and the rudder at the stern controls the direction of movement. **b** The short body and small radius of rotation offer favorable work efficiency

torpedo-type AUV with enhanced propulsive efficiency from a lowered drag coefficient. The hull was designed using the Myring equation, and the optimum nozzle angle (i.e., angle of the tile for the duct part of the hull) was determined based on the shape of the NACA profile (NACA 6721). To validate the design based on CFD analysis, an empirical formula was developed to obtain the drag coefficient for different shapes. This resulted in the design of a duct shape with a low drag coefficient.

In previous research, however, most AUVs were designed through the combination of several already verified representative shapes or from shapes with very few design variables and simple design [8]. However, a universal AUV shape does not exist, and a large number of experiments must be performed if the shape depends on many design variables. Therefore, it is difficult to apply previously researched design techniques to unfamiliar shapes. For example, when designing a shape like the duct-type AUV [1] or duct part alone [7], which have both external and internal shapes, an empirical formula such as the Myring equation cannot be applied because this equation is for the external shape alone. In these cases, the effects inside the through-hole should also be considered because the pressure distribution inside the duct changes depending on the shape of the duct part. When the pressure distribution inside the through-hole is changed, the thrust and drag force are also changed. Therefore, for the optimization of a duct-type AUV like NEMO [1], the design should consider not only the drag but also the thrust. Because there have been few studies on designing both the external and internal shapes, in this study we suggest the following shape design method for effectively optimizing a duct-shape AUV:

- external shape investigation based on Myring equation with cylindrical internal shape
- internal shape investigation using Venturi effect with optimized external shape using Myring equation
- internal shape investigation using Myring equation with optimized external shape using Myring equation.

In the present research, the external and internal shapes of the AUV were independently optimized, as given above. The external shape is designed first to minimize the drag using an empirical formula (e.g., the Myring equation) in the same manner as that described in the existing literature. Then, the internal profile is optimized according to two concepts: considering the Venturi effect and the Myring equation. For the design of the internal profile, the thrust was also examined for the optimization because different pressure distributions occur with different internal hull shapes. To measure the thrust efficiency, we introduced the concept of power consumption. The design factors needed for optimization of the external and internal shapes of NEMO were derived prior to the design. Because the combination of multiple design variables and directly manufacturing and experimenting on all shapes in numerous experiments incurs significant costs and time, numerical analysis was performed using CFD. However, when we were designing the shape analyzed by CFD, the Reynolds number for the fluid used in experimentation was calculated to be very high (i.e., about 140,000 or higher). Under such turbulent conditions, experiments are generally conducted because the resultant values cannot be predicted through ordinary calculation. However, as noted earlier, such experimentation necessitates facilities like a circulating water tank and expensive equipment. Running each experiment requires considerable time for shape fabrication, the actual experiment, and so on. Therefore, the most suitable fluid model was defined by comparing experimental data obtained in earlier experiments [11] with data from CFD analysis to obtain reliable data with high experimental efficiency. However, CFD analysis also takes a relatively long time (i.e., several hours). Therefore, we attempted to increase the efficiency of the CFD analysis by reducing the number of experiments using the Taguchi design method: the experimental results were expressed as a signal-to-noise (S/N) ratio, and the factors that most affect the results were determined. The analyzed results were interpreted to determine the external shape that offers the lowest drag coefficient, and the impact of the drag and thrust based on the internal shape was analyzed. When we optimized the internal and external profiles, the total power consumption was reduced by 7.75 %.

2 External shape optimization using Myring equation

2.1 Myring equation

Myring [9] established the Myring hull profile equation to represent the lowest drag coefficient for a given ratio between the length and maximum diameter of a torpedo-shaped submersible. This equation has primarily been applied to the design of the external shape of a torpedo [7]. Figure 2 presents the NACA profile (NACA 6721), and the Myring equation is given in Eqs. (1) and (2) for the nose, body, and tail sections. Equations (1) and (2) relate the radius r as functions of the nose and tail sections, respectively. The five variables in the equations are the nose section length a, body section length b, maximum diameter length of the hull d, curvature coefficient n, and initial angle of the tail section θ. Once all five variables have been determined, Eqs. (1) and (2) allow the optimum external shape in terms of drag to be determined.

$$r = \frac{1}{2}d\left\{1 - \left(\frac{x-a}{a}\right)^2\right\}^{\frac{1}{n}} \tag{1}$$

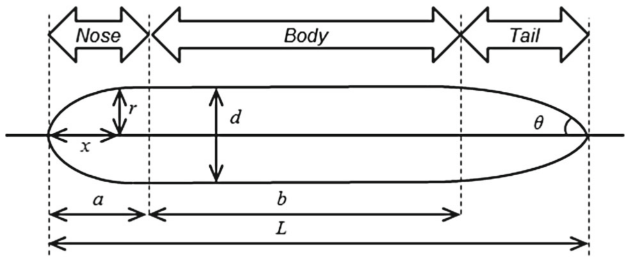

Fig. 2 Variables of Myring equation

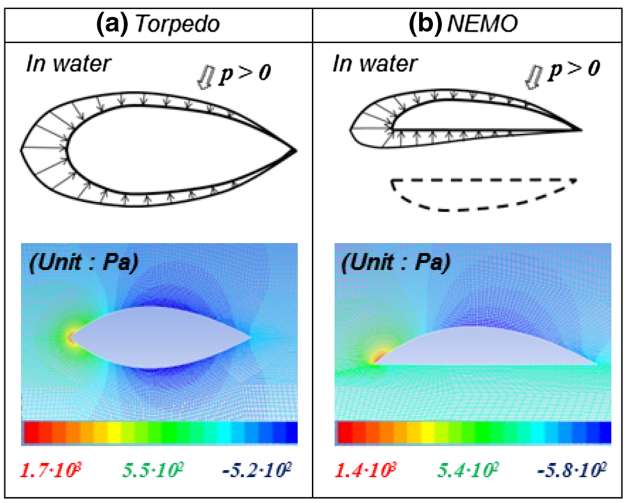

Fig. 3 Pressure distributions of **a** torpedo shape designed with Myring equation and **b** NEMO. The pressure distributions on the external shapes show the same profile

$$r = \frac{1}{2}d - \left\{ \frac{3d}{2(L-a-b)^2} - \frac{\tan\theta}{(L-a-b)} \right\} + \left\{ \frac{d}{(L-a-b)^3} - \frac{\tan\theta}{(L-a-b)^2} \right\} \{x-a-b\}^3 \quad (2)$$

2.2 Selection of variables for design of external shape

In this study, the Myring equation was applied to the external shape design of NEMO. First, we investigated the validity of applying the Myring equation to the external shape design of NEMO. Drag is affected by the pressure and shear stress caused by friction acting on an object's surface. The shear stress occurs along the tangential direction of the surface, and pressure occurs in the normal direction to the surface [10]. Figure 3 shows the pressure distributions on a torpedo designed with the Myring equation and NEMO; the pressure distributions are similar. Thus, if we assume that the shear stresses that occur on the external surfaces are similar and that the shear stress is less than the normal pressure, the external surfaces of the torpedo and NEMO are subjected to similar amounts of drag. When the Myring equation is used to design the external shape of NEMO, the same drag advantages of a torpedo can be obtained.

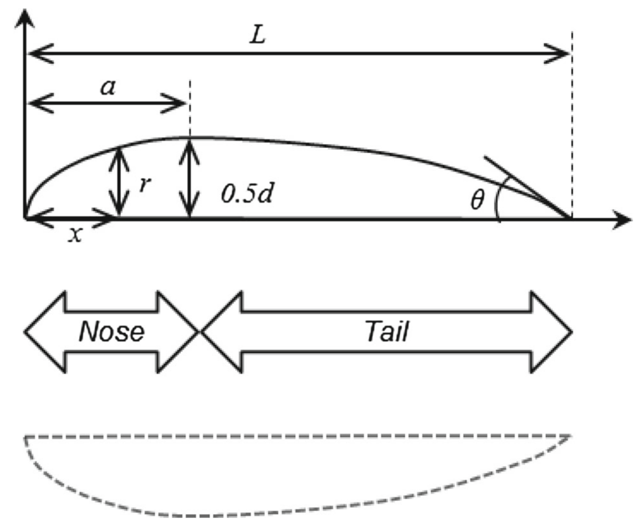

Fig. 4 Variables for NEMO when using Myring equation to design external shape: the total length L, body length b, and maximum radius $0.5d$ were defined as 0.28, 0, and 0.094 m, respectively. Thus, three variables remained to be determined: the nose section length a, curvature coefficient n, and initial angle of the tail section θ

When the Myring equation is applied to NEMO, the size of the through-hole diameter of NEMO must also be considered. Increasing the through-hole diameter increases the overall surface area, which produces a greater drag. When the diameter is too small, this affects the propeller in the through-hole. Thus, the appropriate through-hole diameter needs to be determined. This varies depending on the size of NEMO's propeller. In this study, the through-hole diameter was optimized based on the specifications of an actually fabricated NEMO unit (i.e., inner diameter of 8 cm) [1].

The above results confirmed that the Myring equation can be applied to the external shape design of NEMO. The value of r, which corresponds to the maximum radius of the torpedo, was defined as the distance from the internal surface to the external surface according to the distance of x from the front of NEMO (see Fig. 4). Determining the proper shape for NEMO requires selecting suitable values for the five variables in the Myring equation and determining which will be the design variables. NEMO's hull length is 0.28 m, which is the same value used in the prior study [1]. Because not only the drag but also the work efficiency must be considered, the turning radius should be reduced. The turning radius can be decreased by shortening the hull length, which can decrease the moment of inertia. Therefore, the body length b was determined to be 0. Inside NEMO, modules such as the MCU, battery, sensor, and servo motor occupy certain volumes. Therefore, the maximum radius $0.5d$ was fixed to 0.094 m based on the minimum possible volumes that these modules can occupy. Of the variables a, b, n, θ, and $0.5d$ in the Myring equation, three remained to be determined for their effect on the drag coefficient C_D (Fig. 4): the nose sec-

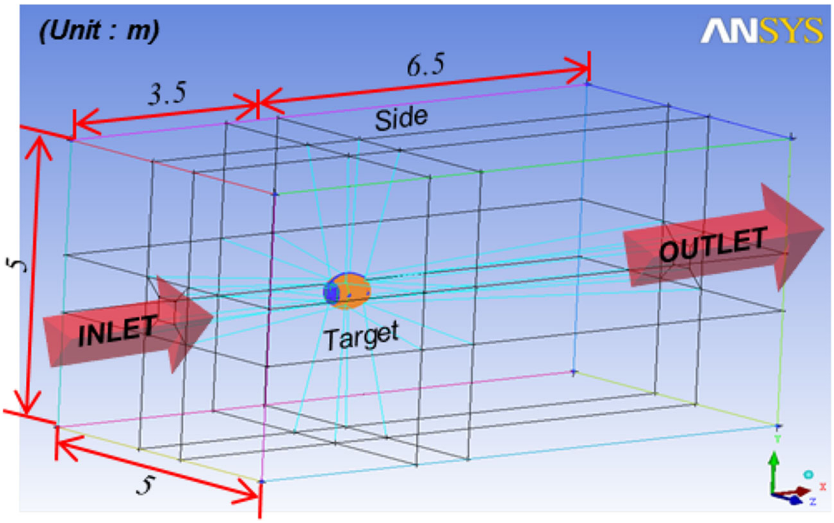

Fig. 5 CFD environment of mesh test

Table 1 Fluid, mesh, and boundary conditions

Fluid, mesh information	
Dimensions	3D
Number of nodes	764,640
Viscous model	Standard k-ε, energy not considered
Material	Water–liquid
Pressure (p)	178.893 Pa
Density (ρ)	998.2 kg/m^3
Viscosity (μ)	0.001003 kg/m s
Reynolds number	140,275
Boundary conditions	
Inlet	Velocity inlet (0.5 m/s)
Side, target	Stationary wall (roughness constant: 0.5)
Outlet	Outlet vent

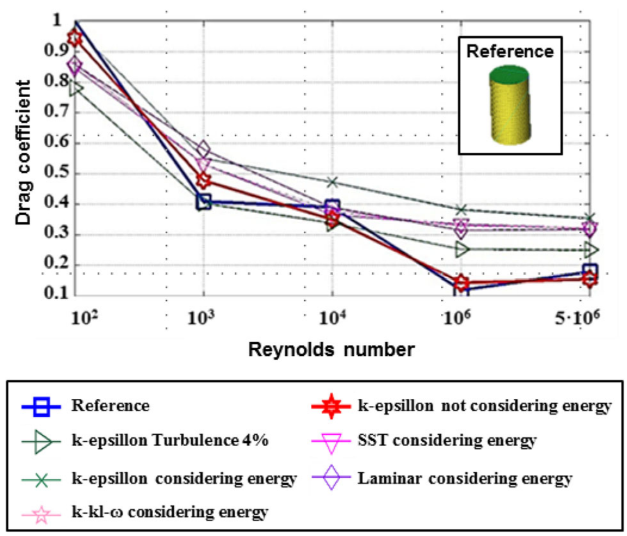

Fig. 6 Mesh test on cylinder: k-ε model not considering energy was most suited to our CFD environment

tion length a (m), curvature coefficient n, and initial angle of the tail section θ (°).

2.3 Selection of fluid model

ANSYS FLUENT 12.1 was used for all CFD analyses in this study. ICEM CFD was used for the meshing process, and FLUENT was used for the analysis. The CFD analysis environment was divided into the inlet, outlet, side, and target, as shown in Fig. 5. The velocity inlet, outlet, side, and target were set as velocity inlet (flow rate of 0.5 m/s), outlet-vent, wall and wall, respectively. In the model, a wall roughness constant of 0.5 was set because the target and water bath in actual experiments should have roughness, which induces friction. As given in Table 1, the Reynolds number for the fluid was more than 140,000. This is very high and denotes turbulent conditions. Thus, the fluid model most suitable for the mesh state must be determined to obtain reliable analytical values using CFD. Determining the most suitable fluid model requires validation through a full comparison between the CFD analysis results and actual experimental data. Blevins [11] measured the drag coefficient values of several shapes at various ranges of Reynolds numbers in actual experiments. Thus, we simply compared the drag coefficient values obtained from the CFD analysis with the experimental values [11] for different Reynolds numbers with a cylinder and different shapes at a specific Reynolds number. This is because the drag coefficient is affected by the Reynolds number and shape.

As shown in Fig. 6, we first checked the tendencies for the drag coefficient of the cylinder over a wide range of Reynolds numbers (i.e., 10^2, 10^3, 10^4, 10^6, 5×10^6) using the CFD analysis and experimental data. We then confirmed that the k-ε model without considering the energy, which is an easily

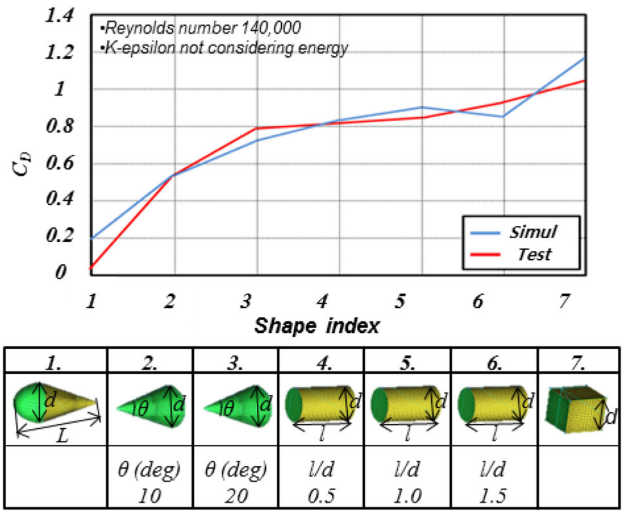

Fig. 7 Mesh test on several shapes: k-ε model not considering energy was found to be suitable

applied and robust engineering model for fluids in multiple flow ranges [7], was the most suited to our CFD environment. As shown in Fig. 7, we then found the tendencies of the drag coefficient for different shapes at the specific Reynolds number of 140,000 based on the k-ε model without considering the energy. Although the CFD analysis values and experimental data were not exactly the same, this model was found to be quite suitable.

2.4 Design optimization using Taguchi method

The Taguchi method [12] is a well-known experimental design approach. If a design has numerous design parameters, a large number of experiments have to be carried out because the various parameters all need to be combined and tested. For example, if there are three design parameters and each design parameter has five values, we have to perform 125 tests in total. This is very inefficient and increases the experimental costs. The Taguchi method uses a special design of orthogonal arrays to study the entire parameter space with a small number of experiments [13]. When all of the experiments are done according to the design parameters listed by orthogonal arrays, the test results are converted to an S/N ratio to measure the quality characteristics that deviate from the desired values. In the Taguchi method, the signal means the desirable value for the output characteristic, and noise means the undesirable values for the output characteristics. Thus, the S/N ratio represents the ratio of desirable test values to undesirable test values in the Taguchi method. There are three kinds of quality characteristics used for analysis of the S/N ratio: the-higher-the-better, the-smaller-the-better, and the-more-nominal-the-better. Regardless of which quality characteristic is used, a greater S/N ratio corresponds to better quality characteristics.

Table 2 Smaller-the-better characteristics of S/N ratio

Characteristic	Smaller-the-better characteristics
S/N ratio	$S/N = 10\log\frac{1}{D}$ $D = \frac{1}{n}\sum_{i=1}^{n} y_i^2$ (y_i : output value)

Table 3 Experimental layout using L_{25} orthogonal array

Exp. No.	Level		
	A	B	C
	a	n	θ
1	1	1	1
2	1	2	2
3	1	3	3
4	1	4	4
5	1	5	5
6	2	1	2
7	2	2	3
8	2	3	4
9	2	4	5
10	2	5	1
11	3	1	3
12	3	2	4
13	3	3	5
14	3	4	1
15	3	5	2
16	4	1	4
17	4	2	5
18	4	3	1
19	4	4	2
20	4	5	3
21	5	1	5
22	5	2	1
23	5	3	2
24	5	4	3
25	5	5	4

Because we wanted smaller values (e.g., drag force and power consumption), we used the-smaller-the-better quality characteristic. Table 2 gives equations for the-smaller-the-better quality characteristic. The Myring equation was used to derive the design variables related to the external shape, as discussed in Sect. 2.2. We derived the three parameters from the Myring equation and each parameter was divided into five levels, as given in Tables 4 and 5. Then, the appropriate orthogonal array should be selected for experiments. Many types of orthogonal arrays exist (e.g., L_4, L_8, L_9, L_{25}). In our case, however (i.e., five levels for each design parameter), our only option was L_{25}. Thus, an orthogonal array with 3 columns and 25 rows was used, as given in Table 3. This

Table 4 First design parameter of external shape

Symbol	Parameter	Unit	Level 1	Level 2	Level 3	Level 4	Level 5
A	*a*	m	0.34	0.355	0.37	0.385	0.4
B	*n*	–	0.6	0.8	1.0	1.2	1.4
C	θ	°	24.0	26.5	29.0	31.5	34.0

Table 5 Second design parameter of external shape

Symbol	Parameter	Unit	Level 1	Level 2	Level 3	Level 4	Level 5
A	*a*	m	0.41	0.42	0.43	0.44	0.45
B	*n*	–	0.86	0.93	1.00	1.07	1.14
C	θ	°	27.4	28.2	29.0	29.8	30.6

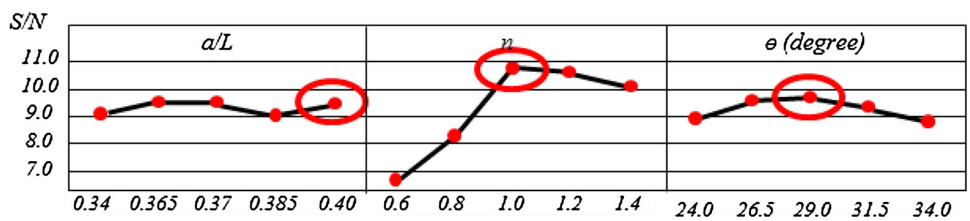

Fig. 8 S/N ratio of first simulation for design of external shape

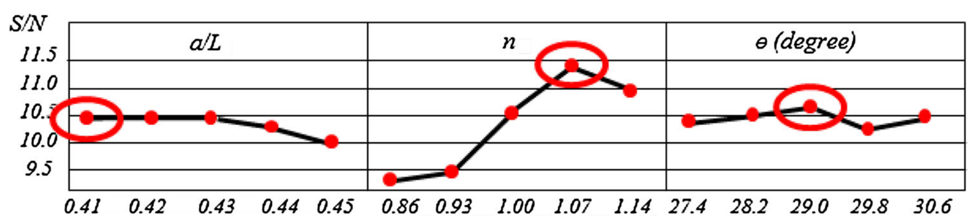

Fig. 9 S/N ratio of second simulation for design of external shape

allowed us to reduce the total number of tests from 125 to 25. After we performed the first 25 tests, the tendencies in the graphed S/N ratio were analyzed and divided into five new levels because the S/N ratio could potentially increase. Then, 25 tests were performed again. In this study, we used the software Minitab 16, which can derive the orthogonal array simply from the number of parameters and levels that we set. We were able to confirm the S/N ratio graph when the experimental results were entered.

2.5 Analysis of the results

The Myring equation was matched with the cross-sectional shape of NEMO in the existing literature [1]. We were then able to derive the parameters of NEMO (i.e., $a = 0.1036$ m, $n = 1$, $\theta = 29°$). The parameters were used as references. The vicinities of the reference parameters were divided into five levels; then, these five parameter levels were selected as the first design parameter of the external shape. Figures 8 and 9 show the results of the first and second CFD analyses using the Taguchi method. In the first test results, smaller-the-better characteristics were expected when a/L was 0.4 or higher, n was 1.0, and θ was 29.0°. Each vicinity was divided into five levels for the second analysis, as discussed in Sect. 2.4. The results showed that the smaller-the-better characteristics were optimized when a/L was 0.41 and n and θ were near 1.07 and 29.0°, respectively. As shown in Figs. 8 and 9, the variation in the S/N ratio for n was greater than that for the others. The results confirmed that the drag coefficient was most affected when n, which is related to the curvature of the external shape, was changed. Through the optimization process using CFD analysis and the Taguchi method, the parameters a, n, and θ were optimized. Table 6 gives the optimized parameters. The external design was optimized (i.e., design parameter of $a = 0.1232$ m, $n = 1.07$, $\theta = 28.2°$), as shown in Fig. 10. Thus, the drag coefficient was reduced by about 12.47 % compared to the reference NEMO (i.e., design parameter of $a = 0.1036$ m, $n = 1$, $\theta = 29°$) in the existing literature [1].

Table 6 Optimized design factors and C_D for external shape

Parameters	*a* (m)	*n*	θ (°)	C_D
Values	0.1232 m	1.07	28.2	0.2526

Figure 1 shows the fabricated NEMO from application of the optimally designed external shape.

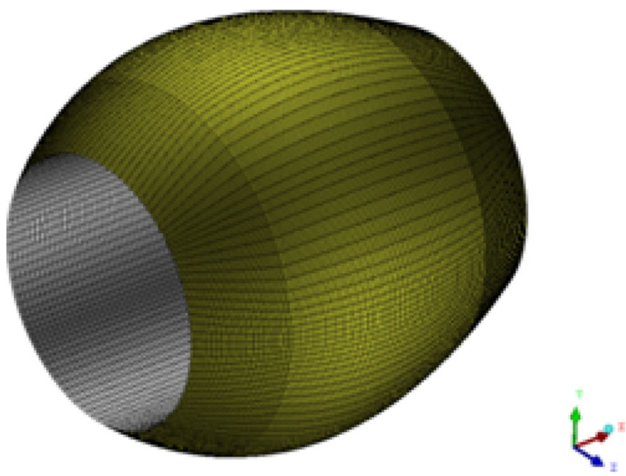

Fig. 10 Mesh for optimal design of NEMO

3 Optimal design of interior shape

The Myring equation was used to optimize the design of the external shape, and the results showed that the drag coefficient could be reduced by about 12.47 % to enhance the propulsive efficiency. To further enhance the propulsive efficiency, the internal shape should be optimized because the external shape of NEMO has already been optimized. The magnitude of the thrust varies depending on the pressure distribution inside the through-hole, so a proper design of the internal shape would make it possible to increase the thrust. The thrust presents an alternative method for improving the propulsive efficiency. A representative method for enhancing the thrust is applying the Venturi effect to the design of the internal shape. When the cross-sectional area of the outlet section through which a fluid flows decreases (such as a nozzle), then the speed of the fluid increases owing to Bernoulli's principle, and the outlet pressure is reduced. Consequently, there is a greater pressure difference between the inlet and outlet Sect. [10], and this phenomenon is responsible for increasing the thrust. However, when the outlet cross-sectional area is decreased, the maximum cross-sectional area of the AUV increases, and eventually the drag also increases. Therefore, we should find an effective shape where the increase in thrust is much larger than the increase in drag. In this study, we sought to find an internal shape that can enhance the thrust without substantially affecting the drag.

3.1 Selection of design variables to consider Venturi effect

Figure 11 shows a schematic view of a Venturi tube. The Venturi tube can be considered to be the most basic form for causing a pressure drop according to the internal geometry. The Venturi effect refers to the pressure drop that occurs owing to Bernoulli's principle when the cross-sectional area of a pathway where a fluid moves through becomes smaller [10]. We applied the Venturi effect to the design of the internal shape of NEMO to verify whether changes in internal geometry can improve the propulsive efficiency (i.e., the increase in thrust is much larger than the increase in drag). The design variables were defined as shown in Fig. 12, which refers to Fig. 11. Design variables 1–3 were defined as Δx, Δy, and the distance from the front of the hull to the propeller of the motor, respectively. Herein, Δx is the distance from the front of the hull to where the x-coordinate of the minimum diameter is located, and Δy is the difference between the maximum and minimum radii of the internal hole.

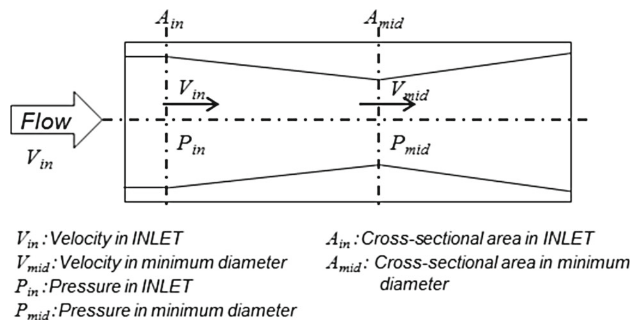

Fig. 11 Schematic view of Venturi tube

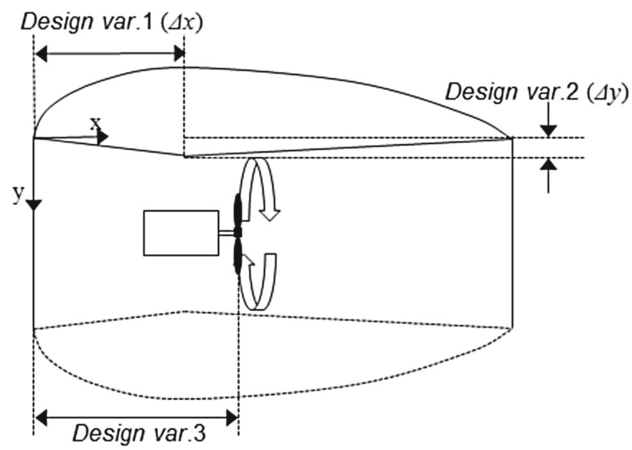

Fig. 12 Design of internal shape considering Venturi effect

3.2 Basic concept to realize dynamic situation from static situation

Designing the internal shape requires a new test method; unlike the external shape test, not only the drag force but also the thrust needs to be considered. When thrust is generated, NEMO moves forward at a constant speed. However, it is difficult to implement a dynamic situation such as NEMO moving forward in a CFD environment. Therefore, the envi-

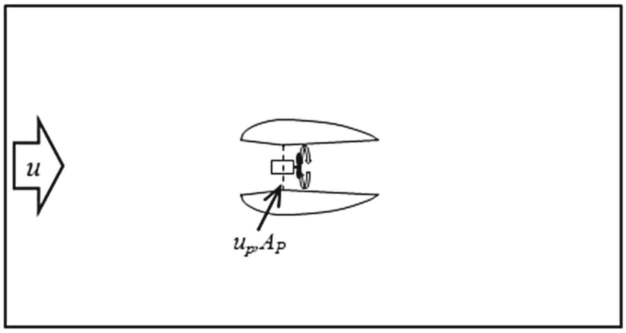

Fig. 13 CFD interpretation environment

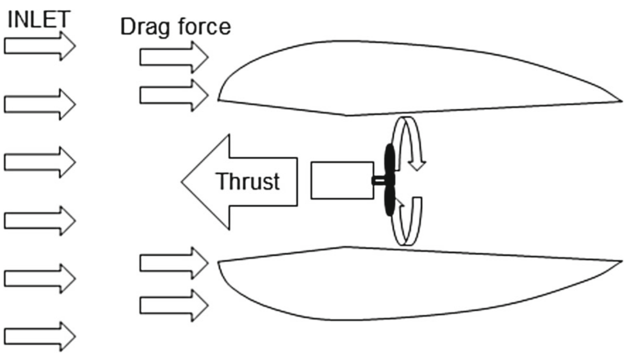

Fig. 14 Thrust and drag force related to AUV

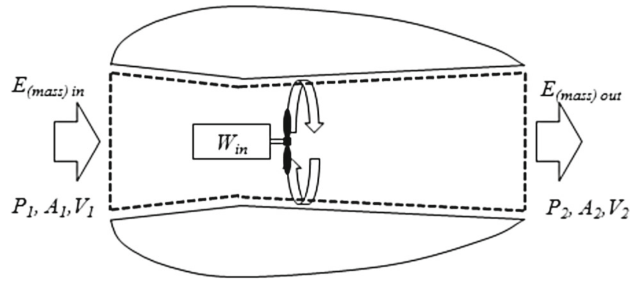

Fig. 15 Schematic view of control box in internal structure of NEMO, energy of mass, and power consumption of motor

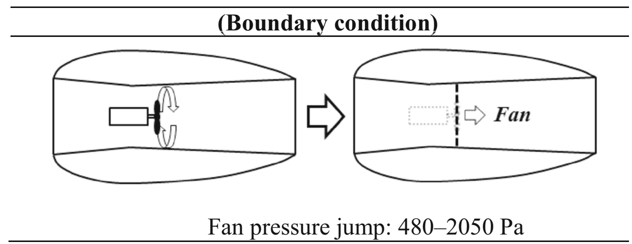

Fig. 16 Fan in FLUENT

ronment was configured to be a static situation similar to a dynamic situation, as shown in Fig. 13. When the same flow rate as the velocity of NEMO is applied at the inlet, as shown in Fig. 14, the drag force is induced toward the direction of the tail section. To maintain its position in one place, NEMO should generate the same thrust as the drag force. In this study, we derived the drag force and thrust by using Eqs. (3) and (4). The drag force was obtained by substituting the drag coefficient C_D found through FLUENT analysis and inserting it with the other values (i.e., density of water ρ, AUV velocity u, which was the same as the velocity of the inlet), and inlet cross-sectional area A into Eq. (3). Similarly, the thrust could be obtained by substituting the mean flow rate at the minimum internal hole diameter for an AUV u_p and inserting it with the other values (i.e., density of water ρ, AUV velocity u, cross-sectional area at the minimum internal hole diameter for an AUV A_{P}) into Eq. (4), as shown in [14].

$$D = \frac{1}{2}\rho u^2 A C_D \tag{3}$$

$$T = 2\rho A_p u_p (u_p - u) \tag{4}$$

3.3 Power consumption

For NEMO to generate thrust, a pressure drop by the propeller is needed. Different internal shapes give different pressure drops even if the same power (i.e., impressed voltage × impressed current) is applied to the motor and identical propellers are used. Therefore, to evaluate the propulsive efficiency for the optimal design of the internal shape, we simply compared the power consumption of the motor when the drag force and thrust were equal. To measure the power consumption of the motor, the internal structure of the NEMO was selected according to the control volume, as shown in Fig. 15. We only considered the energy of the masses; the fluid's internal energy and potential energy were not concerned. The difference between the energies of the masses measured from the input and output of the control volume (i.e., $E_{(\mathrm{mass})\mathrm{in}}$ and $E_{(\mathrm{mass})\mathrm{out}}$) was used to calculate the power consumption of the motor, as shown in Eq. (5). In this equation, V is the mean speed, P is the mean pressure, ν is the kinematic viscosity coefficient of water, and A is the area of the hole at both ends of the control volume. By using these variables, the power consumption could be derived.

$$W_{\mathrm{in}} = V_1 A_1 \left\{ \left(P_2 + \frac{V_2^2}{2\nu} \right) - \left(P_1 + \frac{V_1^2}{2\nu} \right) \right\} \tag{5}$$

3.4 CFD analysis

ANSYS 12.1 FLUENT was employed for the CFD analysis, just like with the external shape design. To reduce the number of tests, the Taguchi design of experiments was applied, similar to that described in Sect. 2.5. The resulting power consumptions of the motor were compared through CFD analysis. Minimizing this value increases the efficiency of

Table 7 First design parameter for internal shape considering Venturi effect

Symbol	Parameter	Unit	Level 1	Level 2	Level 3	Level 4	Level 5
A	Δx	m	0.0467	0.0933	0.14	0.187	0.233
B	Δy	m	0.012	0.014	0.016	0.017	0.02
C	Motor position	m	0.03	0.06	0.09	0.12	0.15

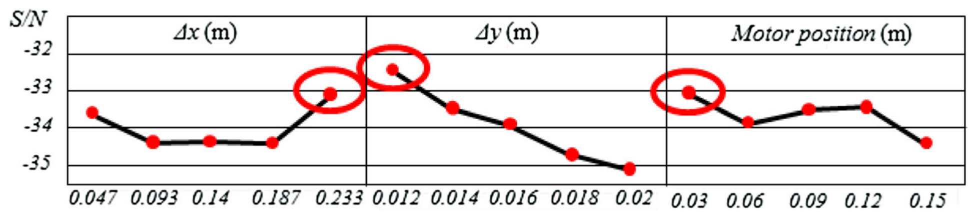

Fig. 17 S/N ratio of first simulation for design of internal shape considering Venturi effect

Table 8 Second design parameter for internal shape considering Venturi effect

Symbol	Parameter	Unit	Level 1	Level 2	Level 3	Level 4	Level 5
A	Δx	m	0.241	0.249	0.257	0.265	0.272
B	Δy	m	0.002	0.004	0.006	0.008	0.01
C	Motor position	m	0.0287	0.0289	0.029	0.0292	0.0293

Table 9 Optimized design factors for internal shape using Venturi effect and power consumption

Parameters	Δx (m)	Δy (m)	Prop. (m)	Power consumption (W)
Values	0.2489	0.004	0.029	28.13

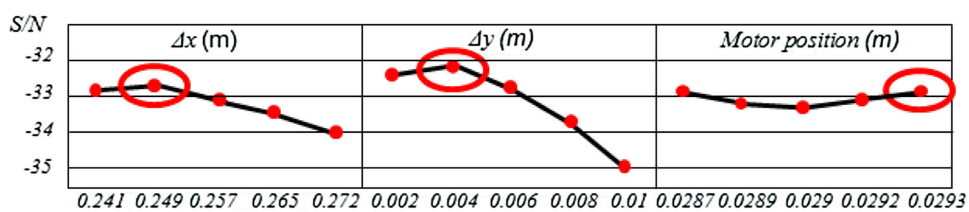

Fig. 18 S/N ratio of second simulation for design of internal shape considering Venturi effect

the design, so smaller-the-better characteristics were applied in the analysis, similar to the external shape optimization design process described earlier.

All testing conditions were as given in Table 1 except for a fan function, which was added to implement the propeller in FLUENT, as given in Fig. 16. The fan was used to apply a pressure jump of 480–2050 Pa. The values varied depending on the internal shape. The first parameters were arbitrarily chosen with the purpose of simply confirming the feasibility of this approach. The vicinities of these parameters were then divided into five levels, and these five levels of parameters were selected according to the first design parameter of the internal shape, as given in Table 7.

3.4.1 Results analysis

The design optimization process was very similar to that of the external design. First, we ran the CFD analysis 25 times using the design parameters given in Table 7. Figure 17 shows the main effects of the S/N ratio on the resulting values. The most favorable smaller-the-better characteristics appeared when Δx was around 0.2334 m. However, the graph showed an increasing tendency even when Δx was 0.0467 m, so an additional CFD analysis needed to be run. The CFD analysis was thus implemented by dividing the regions of 0.0467 and 0.2334 m into three factors. The analysis results showed that the S/N ratio graph had the same tendencies as the previous graph. When Δx was 0.2334 m or greater, the S/Nratio was confirmed to increase by an even larger width. Thus, a secondary design factor was designed by dividing the vicinity where Δx was 0.2334 m into five levels again. The graph analysis results showed that Δy and the propeller position had more favorable smaller-the-better characteristics when positioned closer to the tail section, so a secondary design factor was defined by dividing the tail section vicinity into five stages again, as shown in Table 8. When the newly designed parameters served as the basis for the secondary analysis, the results showed that $\Delta x =$ 0.2489 m, $\Delta y = 0.004$ m, and the propeller position = 0.029 m exhibited the best propulsive efficiency. Table 9 gives the parameters and power consumption derived from the analysis. When the internal shape of NEMO was designed like

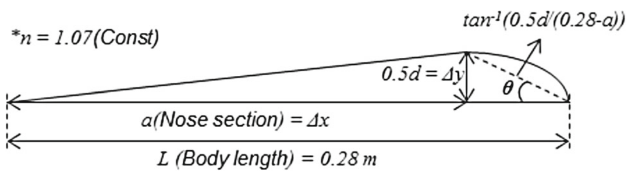

Fig. 19 Myring design variables

a Venturi tube, the power consumption was about 28.13 W when the AUV moved forward at a speed of 0.5 m/s. This was a 7.75 % reduction in power consumption compared to when only the design of the external shape was optimized (Fig. 18).

3.5 Selection of design variables considering Myring equation

As described above, considering the Venturi effect for the design of the internal shape was confirmed to reduce the power consumption. We then considered whether designing the Venturi tube shape with streamlines will improve the propulsive efficiency because of the drag reduction. Thus, the Myring equation was used to design the internal shape. To derive the variables, we simply matched the parameters used in the internal shape design considering the Venturi effect to the Myring equation, as shown in Fig. 19. Thus, Δx, Δy and θ were substituted with a, $0.5d$, and $\tan^{-1}(0.5d/(0.28-a))$, respectively, in the Myring equation. n was fixed to 1.07, which was the curvature coefficient that showed the lowest drag coefficient in the external shape optimization (Tables 10, 11). When the internal shape was designed with the Myring equation, three parameters were considered: a , $0.5d$, and the motor position.

3.5.1 Results analysis

Similar to the previous tests, the design was optimized using the Taguchi method. Figure 20 shows the main effects of the S/N ratio in the first CFD analysis. Δx tended to increase both below 0.0467 m and above 0.2334 m. Each vicinity was divided into three factors, similar to the internal shape design when the Venturi effect was considered, and additional CFD analyses were performed. In the results, Δx showed even better smaller-the-better characteristics in the vicinity of 0.0467 m, and this vicinity was divided into five levels to define the secondary design factors (Fig. 21). Similar to the internal shape design considering the Venturi effect, Δy and the propeller position exhibited better smaller-the-better characteristics toward the nose section vicinity, so each vicinity was divided into five levels to specify the secondary design factors again. When the secondary factors served as the basis for analysis, the results showed that $\Delta x = 0.0233$ m, $\Delta y = 0.002$ m, and propeller position = 0.029 m yielded the best propulsive efficiency, as given in Table 12. When NEMO with a streamlined internal design using the Myring equation was moved forward at a speed of 0.5 m/s, the power consumption was about 30.44 W. This was a reduction of 0.1766 % compared to the power consumption of NEMO when only the external shape was optimized, as given in Table 12.

3.6 Comparison and interpretation of CFD analysis results

Table 13 presents the CFD analysis results for NEMO when the Venturi effect and Myring equation were considered for the internal design. Different CFD analysis results were

Table 10 First design parameter of internal shape considering Myring equation

Symbol	Parameter	Unit	Level 1	Level 2	Level 3	Level 4	Level 5
A	Δx	m	0.047	0.093	0.14	0.187	0.233
B	Δy	m	0.012	0.014	0.016	0.018	0.02
C	Motor position	m	0.03	0.06	0.09	0.12	0.15

Table 11 Second design parameter of internal shape considering Myring equation

Symbol	parameter	Unit	Level 1	Level 2	Level 3	Level 4	Level 5
A	Δx	m	0.008	0.016	0.023	0.031	0.039
B	Δy	m	0.002	0.004	0.006	0.008	0.01
C	Motor position	m	0.0287	0.0289	0.029	0.0292	0.0293

Fig. 20 S/N ratio of first simulation for internal shape design optimization considering Myring equation

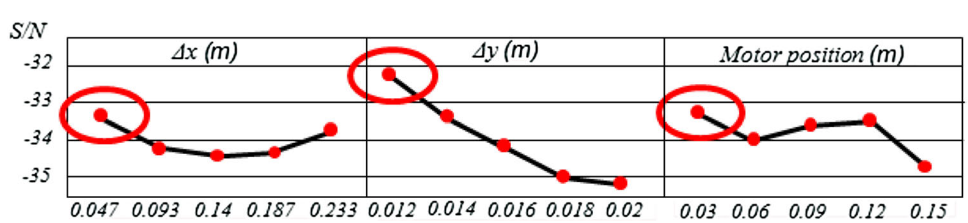

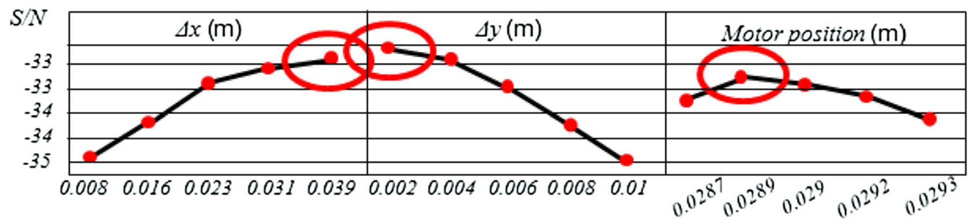

Fig. 21 S/N ratio of second simulation for internal shape design optimization considering Myring equation

Table 12 Internal shape optimization design factors using Myring equation and power consumption

Parameters	Δx (m)	Δy (m)	Prop. (m)	Power consumption (W)
Values	0.023	0.002	0.029	30.44

Table 13 Simulation results comparing internal shapes of NEMO when considering Myring equation and Venturi effect

	Cylindrical shape	Considering Myring equation	Considering Venturi effect
Drag force (N)	0.17	0.1614 (3.99 % ↓)	0.1659 (1.31 % ↓)
Thrust (N)	0.23	0.2218 (3.39 % ↓)	0.2301 (0.21 % ↓)
Power consumption (W)	30.49	30.439 (0.177 % ↓)	28.1304 (7.75 % ↓)
$\Delta x/\Delta y$/motor pos. (m)	–	0.0233/0.002/0.029	0.2489/0.004/0.029

compared with NEMO when only the external shape was optimized, and the changes in power consumption are given in the table as percentages. The efficiencies of each shape were analyzed in terms of the drag force. The drag force was reduced by about 4 % in NEMO with a streamlined internal design that considered the Myring equation. The drag was reduced by 1.31 % in NEMO with a nozzle-shaped internal design considering the Venturi effect. Thus, designing NEMO's internal shape according to the Myring equation is more efficient in terms of drag. Next, the efficiency of the shapes in terms of thrust was analyzed. In the analytical results, the thrust was actually reduced by 3.39 % in NEMO with a streamlined design that considered the Myring equation for the internal shape. In contrast, NEMO with a nozzle-shaped internal design that considered the Venturi effect had a thrust increase of about 0.21 %. This shows that a nozzle-shaped internal design considering the Venturi effect was more efficient in terms of thrust. As given in Table 13, both shapes reduced the power consumption, so the propulsive efficiency was increased. This is because the increase in drag was smaller than the increase in thrust. Therefore, when considering the thrust to optimize the shape of the AUV, emphasis should be placed on increasing the thrust relative to the increase in drag rather than on the absolute increase in thrust.

4 Conclusion

In this study, the external and internal shapes of the duct-type AUV NEMO were optimized. The Myring equation, which is primarily used for torpedo-type submersible designs, was applied to define the design factors needed for an optimally designed external shape. An optimal design was implemented by simplifying the variables and considering the applicability of the Myring equation to NEMO. The derived results confirmed that the drag coefficient was reduced in comparison to the conventional forms. In the optimization of the internal shape, the design factors were defined using the Venturi effect and Myring equation, and both the drag and thrust were considered. Many tests must be run when all of the factors defined in the optimization design are combined. To reduce the number of tests efficiently and save on time and costs compared to actual experimentation, the Taguchi method was used with CFD analysis for design optimization. A nozzle-shaped internal design considering the Venturi effect produced better thrust results, while that using the Myring equation to develop a streamlined internal design produced better drag results. The results showed that using the Taguchi method on CFD analysis allows the efficient design of unmanned submersible shapes in terms of time and cost.

Acknowledgments This research was a part of the project titled 'R&D center for underwater construction robotics', funded by the Ministry of Oceans and Fisheries (MOF) and Korea Institute of Marine Science & Technology Promotion (KIMST), Korea (No.2013019713).

References

1. Kang B-G, Kim J (2011) Development of ducted single thruster unmanned underwater vehicle. Korea Robot Soc (KROS) 6:143–145
2. Kim C, Choi D-H (2011) Development of technology for optimized wing design of subsonic aircraft. Korea Aerosp Res Inst (KARI) 10(1):175–182
3. Kwon HI, Ryu DO, You JY, Kwon OJ (2011) Aerodynamic sectional design optimization of wind turbine rotor blade considering

elastic structure deformation. The Korean Society for Aeronautical & Space Sciences (KSAS), pp 1276–1283
4. Palmisano J, Ramamurti R, Lu K-J, Cohen J, Sandberg W, Ratna B (2007) Design of a biomimetic controlled-curvature robotic pectoral fin. In: IEEE international conference on robotics and automation, pp 966–973
5. Park Y-S, Kim W-J, Jun B-H (2012) Flow analysis around multi-legged underwater robot "Crabster" to evaluate current loads. Korean Soc Ocean Eng (KSOE) 26(5):47–54
6. Inoue T, Suzuki H, Kitamoto R, Watanabe Y, Yoshida H (2010) Hull form design of underwater vehicle applying CFD. In: OCEANS 2010 IEEE-Sydney, pp 1–5
7. Jung T-H, Karl S, Fangpo H, Lee S-K (2012) Shape optimization of an autonomous underwater vehicle with a ducted propeller using computational fluid dynamics analysis. Inter J Nav Archit Ocean Eng (JNAOE) 4(1):45–57
8. Stevenson P (2007) AUV shape-combining the practical and hydrodynamic considerations. In: OCEANS 2007-Europe, pp 1–6
9. Myring DF (1976) A theoretical study of body drags in subcritical axisymmetric flow. Aeronaut Q 27(3):186–194
10. White FM (2012) Fluid mechanics 7/E. McGraw-Hill, New York
11. Blevins RD (1984) Applied fluid dynamics handbook. Van Nostrand Reinhold, New York
12. Taguchi G (1986) Introduction to quality engineering: designing quality into products and processes. Quality Resources, Tokyo
13. Yang WH, Tarng YS (1998) Design optimization of cutting parameters for turning operations based on the Taguchi method. J Mater Process Technol 84:122–129
14. Kim J, Chung WK (2007) Thruster modeling for underwater vehicle with ambient flow velocity and its incoming angle. Korea Robot Soc (KROS) 2:109–118